2024 IEEE International Conference on Robotics and Automation (ICRA 2024)
May 13-17, 2024. Yokohama, Japan

Co-Axial Slender Tubular robot (CAST): Towards Robotized Operation for Transorbital Neurosurgery with Minimal Invasiveness

Shuai Wang, Qingxiang Zhao, Jian Chen, Mingcong Chen, Guanglin Cao
Jian Hu, Runfeng Zhu, Danny Tat Ming Chan, Ming Feng and Hongbin Liu

***Abstract*— Transorbital Neuro Surgery (TNS) offers a novel treatment towards the lesion inside skull pursuing minimal invasiveness. Most conventional TNS tools are rigid and straight, limiting the dexterity and accessibility in passing a small port. Bendable and steerable surgical tools provides an alternative for this issue. In this work, we proposed a dual-segment slender surgical robot arm for TNS, which is a Co-Axial Slender Tubular robot (CAST), and modelled it using novel approaches. Another contribution is tendon-mortise shaped slits along the axial direction, enhancing the overall stiffness. The bending of CAST is actuated by pushing/pulling distance, and the maximum diameter is only $1.7mm$ with high dexterity after mounting on a rigid robot arm. Experiments demonstrates that the proposed the slit design doubles the stiffness properties compared to traditional rectangle slit designs. The path-following task shows that the position error was maximally $3mm$ in open-looped control. Test on a skull model demonstrates that the whole system could successfully perform electrocoagulation procedure inside the depth of skull in a robotized manner effectively.**

I. INTRODUCTION

Transorbital neurosurgery (TNS) is a novel surgery, requiring surgical tools to access the orbit and intracranial area [1], [2]. It allows visualization and operate above the skull base [3], [4]. At present, a surgeon holds an endoscope and a suction tube at the left hand, and delicately steers a surgical tool to manipulate, like a forceps and electrode, which causes inconvenience especially at the left hand. More importantly, the endoscope and suction tube are generally rigid and straight, posing challenge in accessing depth of the lesion. Sometimes, an assistant or more surgeons are needed. Robotics system offers a potential solution for this issue.

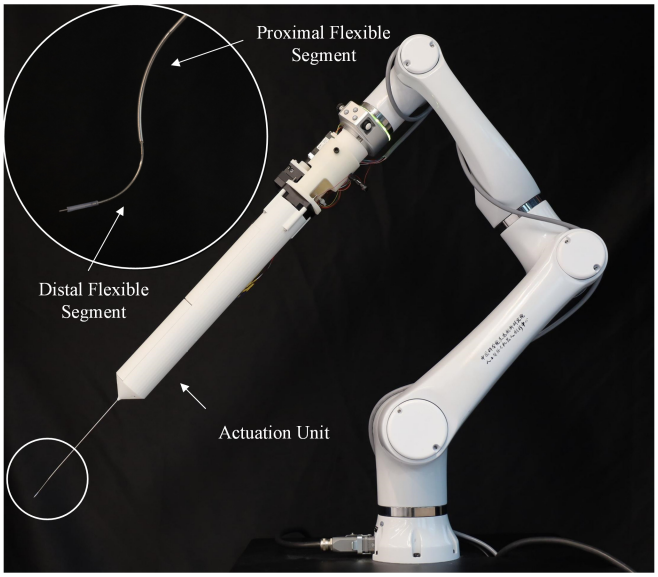

Fig. 1. System setup. A rigid robot arm holds the dual-segment co-axial surgical tool and can be positioned dexterously in narrow space.

Bendable and steerable continuum robots are advantageous [5]. In this work, our aim is to propose a fully robotized surgical tool for TNS while pursing minimal invasiveness using a dual-segment flexible robot arm.

The first key requirement is small size in diameter [6]. Continuum robots characterize slender body and high ratio of length to diameter, and they are widely applied in inspection [7] and Minimally Invasive Surgery (MIS) [8], [9]. Their key working principle is individual elongation and shortening of the secondary backbones, for whichever tendon-driven or fluid-driven mechanisms. Magnetically-actuated continuum robots and concentric robots are advantageous in cross-section dimension [10], while they either require bulky actuators or are not compatible with ferromagnetic environments. Tendon-driven continuum robots are common in continuum robotics [11]. Pin hinge joints [12], rolling joints [13] and spherical joints [14] in this design have realized 2D or 3D bending. Spring or spring-based structures were also embedded into tendon-driven continuum robots. A slender elastic rod is typically needed to keep the backbone length [15]. But there also exists difficulty in designing flexible tools $\leq 2mm$ in diameter.

The second requirement is sufficient stiffness to maintain its shape while interacting with surroundings, such as bones and tissues, which is generally contradictory with small

This work was supported by InnoHK Programme, Hong Kong, and partially supported by Sichuan Science and Technology Program (Grant number: 2023YFH0093). (Corresponding author: Hongbin Liu)

Shuai Wang and Qingxiang Zhao are with the centre for Artificial Intelligence and Robotics (CAIR), Hong Kong Institute of Science and Innovation, Chinese Academy of Sciences. ({shuai.wang,qingxiang.zhao}@cair-cas.org.hk).

Jian Chen and Guanglin Cao are with the School of Artificial Intelligence, University of Chinese Academy of Sciences, Beijing 100049, China, also with the State Key Laboratory of Multimodal Artificial Intelligence Systems, Institute of Automation, Chinese Academy of Sciences (CASIA), Beijing 100190, China (chenjian2020@ia.ac.cn).

Mingcong Chen is with Department of Biomedical Engineering, City University of Hong Kong, HKSAR (mingcchen5-c@my.cityu.edu.hk).

Runfeng Zhu is with the Department of Mechanical Engineering, The Hong Kong Polytechnic University. (22063957g@connect.polyu.hk)

Danny Tat Ming Chan is with Department of Surgery, The Chinese University of Hong Kong, HKSAR (tmdanny@surgery.cuhk.edu.hk)

Ming Feng is with the Beijing Union Medical College Hospital.(jackietz@163.com)

Jian Hu and Hongbin Liu are jointly with CAIR and CASIA. (hujian@cair-cas.org.hk,liuhongbin@ia.ac.cn) Corresponding Author: Hongbin Liu.

size. To this end, particle jamming [16], low-melt-point alloy [17], and antagonistic mechanism [18] were employed to regulate the stiffness of continuum robot arms. They either requires much heating/cooling time or complicated structures, and are not able to be fabricated within ultra-slender body. In this work, we proposed a dual-segment Co-Axial Slender Tubular (CAST) robot arm for TNS on the basis of a push-pull design [19], [20]. Although it only provides bidirectional bending by relative translation of the two tubes, large ration of inner diameter to outer diameter is beneficial for instrument channel. Additionally, it does not require hollow space for actuation. On the other hand, patterned tubes has smaller second moment of inertia, so that the stiffness is relatively smaller. In this work, we proposed a tendon-mortise mechanism on the patterned slits. Once the tendons and mortises are buckled together, larger stiffness could be achieved.

The third issue is manipulability and positioning accuracy during surgery [10]. Modeling between actuation configuration (AC) to task space (TS) is fundamental. In continuum robotics, robot shape assumed as arches connected in series, generally acts as a bridge between the actuators and tip pose. Piecewise constant curvature and variable curvature model are popular [21], but they are not accurate in dealing with external disturbances. Researchers also investigated pseudo-rigid-bar model [22], cosserat rod theory and dynamics [23] to model the basic control law, while they need much computational resource or accurate actuation forces. For ultra-slender continuum robots, embedded sensors also occupies hollow instrument channel [24]. In this work, we considered geometry-based approach to build the forward kinematics, and optimization-based method to solve the inverse kinematics, where an key parameter was extracted to properly regulate the robot shape.

Compared with most existing flexible surgical robots, our design characterizes smaller diameter and higher stiffness. In terms modeling and controlling, easier approach was proposed to target at fully robotized surgery and slave-master form control. As a result, CAST has the following characteristics:

- The maximum diameter of the surgical robot is only $1.7mm$, leaving an instrument channel of $0.6mm$.
- Novel tendon-mortise pattern has been proposed and validated to significantly enhance the overall stiffness.
- Assembled on a six-DoF rigid robot, CAST could perform articulate motion with the kinematics modeling.
- Initial testing has demonstrated its dexterity and robustness on TNS.

This rest of this paper is organized as follows. In section-II, we introduced the basic working principle of the surgical robot arm and design of the entire system. Modeling including forward and inverse kinematics has been clarified in section-III. Section-IV validated the stiffness of the design, motion accuracy and practicability in TNS. Finally, section-V concluded this work and illustrates future work.

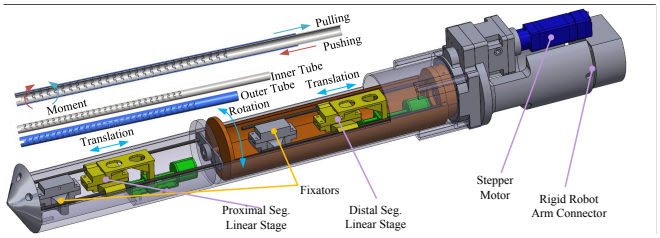

Fig. 2. CAD model of the design. Two tubes were asymmetrically patterned at the cross section, and then they were fixed at the tip. Relative axial translation deforms robot arm. The actuation unit generates push/pull displacement for the inner tubes and rotation for the distal segment.

TABLE I

KEY DESIGN PARAMETERS OF THE SURGICAL ROBOT.

	Dis. Seg. (D)		Prox. Seg. (P)	
	Inner Tube	Outer Tube	Inner Tube	Outer Tube
Rigid length (mm)	523	464	290	260
Steerable length (mm)	30	30	40	40
ID (mm)	0.6	0.9	1.2	1.5
OD (mm)	0.8	1.1	1.4	1.7
Uncut section angle (°)	36	36	20	45
Slit width (mm)	0.03	0.03	0.03	0.03

II. SYSTEM DESCRIPTION

For transorbital neurosurgery, the surgical tools should be small enough to access the orbit with comparable stiffness for surgical procedures, such as dissection and suction. Our aim is to propose a flexible surgical arm adapting common tools. Take a flexible endoscope as an example. Smaller diameter will contribute to larger task space of other tools.

Unlike conventional tendon-driven continuum robots, we adopted push-pull actuation method for steering. As shown in Fig. 2, one segment of robot arm consists of two asymmetrically patterned tubes assembled coaxially with each other. They have a shift angle of $180°$. Once fixing the outer tube, pushing (pulling) force along the inner tube generates an inward (outward) moment, which leads to bidirectional bending of the whole arm. Work [20] proposed this design in 2017, while it has marginal stiffness in application. We update the patterned slits by using tendon-mortise mechanism, such that tendons will buckle with mortises to provide tension, enhancing the overall stiffness. Consequently, the ratio of inner diameter to the outer is much higher than conventional designs, because the thin-walled structure contributes to force transmission. In general, 3D bending is preferred in application, so a revolve DoF is added at the rigid section of the tubes, enabling full rotation. For dexterity, we designed a dual-segment surgical arm, where the distal one passes through the proximal, as shown in Fig. 2. The outer tubes are all fixed in the actuation unit, and the inner tubes of each segment were respectively pushed/pulled by two linear stages.

The actuation is mounted at the end effector of a rigid robot arm (Elfin E05, Han's Robot, Shenzhen, China). The distal segment's rotation is achieved by a stepper motor, and that of the proximal segment is due to robot arm. As a result, the whole system has totally 9 DoFs. Some key design parameters are listed in Table I.

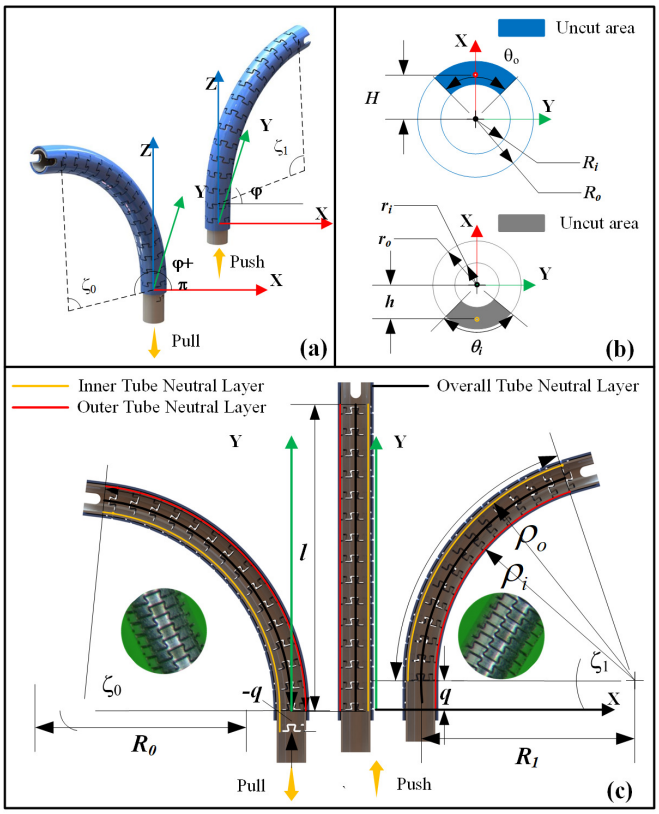

Fig. 3. Modeling. (a) Pushing and pulling the inner tube generates bidirectional bending. (b) Cross section of the two tubes, and the uncut areas have a shift angle of 180°. (c) Actuation input q and the bending angle ζ are directly related.

III. Modeling

Modeling one segment of the robot is the key to control the tip position, including forward kinematics and inverse kinematics. In modeling, only the mapping between actuation unit and tip pose was considered as rigid robot control is sophisticated.

A. Single Segment Bending

The deformation of one single segment depends on the relative translation between the inner tube and the outer tube, so the mapping between the distance q is highly involved in the bending angle. Herein, considering the densely distributed patterns (around $0.2mm$ gap between adjacent slits), we assume the shape of the robot is an arch with constant curvature. Because of its essential feature, pushing and pulling the inner tube while the outer tube is fixed generates bidirectional bending. Let $q > 0$ be the push configuration and $q < 0$ denotes pulling the inner tube. l is the length of bendable section.

During bending, the neutral layer of each tube keeps constant length, and the distance from the neutral layer to the centre is:

$$h = \frac{a_o y_o - a_i y_i}{a_o - a_i} \tag{1}$$

where $a_o = \frac{\theta_0}{2} R^2$ and $a_i = \frac{\theta_0}{2} r^2$ are respectively the area of sectors. y_o and y_i are their neutral layer distance to the centre.

Furthermore, the bendable section of inner tube and the outer tube has the same length. Therefore, two scenarios should be considered: 1) While the inner tube is being pushed by q, the length of bendable section is $l - q$ because rigid part of the inner tube with a length of q is embedded into the bendable section of the outer tube, as shown in Fig. 3 (c-right); and 2) While it is being pulled, the bendable section length is l, illustrated in Fig. 3 (c-left). For whichever scenario, there is a deviation between the length of inner tube's neutral layer length and outer tube's neutral layer length q, but they share the identical centre of arch when in bending.

1) Pushing Actuation. In this scenario $(q > 0)$, the bending radius w.r.t. the neutral layer of the two tubes are:

$$\begin{aligned} \rho_o &= (l - q)/\zeta_1 \\ \rho_i &= l/\zeta_1 \end{aligned} \tag{2}$$

where ρ_o and ρ_i respectively denote the bending radius of the outer tube and the inner tube. With the geometry, the deviation between ρ_o and ρ_i is equal to the sum of the H and h: $\rho_o - \rho_i = H + h$. So, the bending angle ζ_1 is solved as:

$$\zeta_1 = \frac{q}{H + h} (q > 0) \tag{3}$$

2) Pulling Actuation. Similarly, the bending radii ρ_o, ρ_i of the tubes are derived as:

$$\begin{aligned} \rho_i &= (l + q)/\zeta_0 \\ \rho_o &= l/\zeta_0 \end{aligned} \tag{4}$$

where $q < 0$ and the bending angle is ζ_0. The pulling actuation q has a mapping with ζ_0:

$$\zeta_0 = \frac{-q}{H + h} \tag{5}$$

Pulling or pushing also determines the bending direction, so $sign(\cdot)$ could be used to map between q and the direction angle 0 or π: $\varphi_m = 0.5(sign(q) + 1)\pi$.

B. Forward Kinematics

Now, the shape parameter of one segment includes: backbone length l, rotation angle φ, bending direction φ_m and bending radius ζ. With the shape parameters of the two segments and the robot translation Q, the tip pose w.r.t. robot base could be solved via Homogenous Transformation matrix:

$$\begin{aligned} &T = T_z(Q) R_z(\varphi_p + \varphi_{mp}) T_z(l_p/\zeta_p) R_z(\zeta_p) T_x(-l_p/\zeta_p) \\ &R_z(\varphi_d + \varphi_{md}) T_z(l_d/\zeta_d) R_z(\zeta_d) T_x(-l_d/\zeta_d) \end{aligned} \tag{6}$$

where subscript d and p respectively denote the parameter of the distal segment and the proximal segment. T_i and R_i respectively denotes translation and rotation about i axis.

C. Optimization-based Inverse Kinematics

In this push-pull actuation mechanism, the actuation inputs should be well solved to bring the robot to a desired tip pose. Since the orientation and position is coupled for the dual-segment design, the inverse mapping is build for finding an

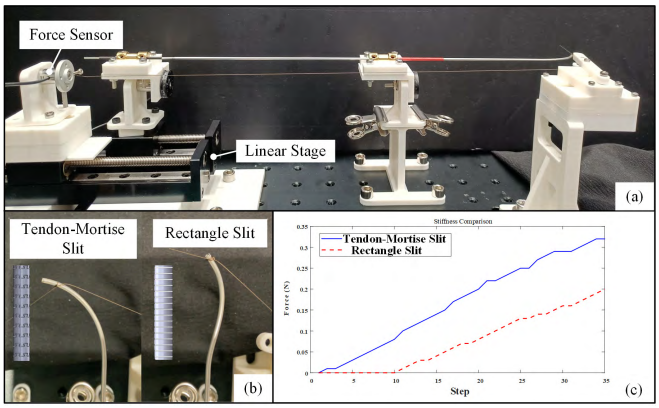

Fig. 4. Stiffness Comparison. (a) Experiment setup. A linear stage pushes the inner tube to generate bending, and a steel wire connects the tip and a commercial force transducer. (b) Shape comparison between the two designs under the pushing distance of $20mm$. (c) Push distance and generated force relationship.

actuation inputs A_d for a given desired position P_d. Because of the redundancy, it is difficult to find A_d directly. We consider an optimization-based approach.

With (6), the forward kinematics could be denoted as: $P = f(A)$, where actuation inputs $A = [Q, q_p, \varphi_p, q_d, \varphi_d]$. In optimization model, the error between given position P_d and solved position should be minimized satisfying some physical constraints:

$$\min . \|P_d - f(A)\| \quad S.t. \begin{cases} 0 \leq q_p, q_d \leq q_{\max} \\ Q_{\min} \leq Q \leq Q_{\max} \\ 0 \leq \varphi_p, \varphi_d \leq 2\pi \end{cases} \tag{7}$$

The first constraint the push/pull distance, limiting the maximum bending angles. The second constraint denotes the translation space of rigid robot end effector, and the third one is to limit rotary DoF. The presence of $sgn(\cdot)$ leaves challenge in finding the gradient of the loss function, so we employed an iteration algorithm, Genetic Algorithm (GA), to find the optimal actuation inputs. In GA, The population size was set to 50, and the maximum generation in iteration was 200.

Actually, the rotation of the distal segment enhances the dexterity. Physically, it could still reach a desired position if the rotation DoF of the distal segment is deactivated, which constrains CAST to bend in a 2D manner. Namely, by setting $\varphi_d = 0$, GA quickly reaches convergence.

IV. Experimental Validation

In this section, experiments for giving compelling evidences that improving robot stiffness, maneuverability, accuracy and practicability is presented.

A. Stiffness Comparison

One of the key contributions in this work is tendon-mortise slit design. The first experiment is to compare the stiffness enhancement with conventional rectangle slits design. Fig. 4 (a) shows the experimental setup. The proximal segment was used for comparison, and only the silt types are different. One linear stage pushes/pulls the inner tube to generate bending, and a wire is fixed at the tip to generate external disturbance. The other end of the wire is connected to a single-axis force sensor (SBT671-100N, SIMBATOUCH, Guangzhou, China) to measure the force. The linear stage gradually pushed the inner tube, and the sensor readings were simultaneously collected for comparison. Intuitively, larger force means higher bending force was generated. In Fig. 4 (b), there is a clear deformation for the rectangle slits design, and the tendon-mortise slit design almost keeps its arch shape. Fig. 4 (c) shows the variation between push distance and force, where push distance gap was $0.1mm$ in each step. In the initial 10 steps, the deformation of the rectangle slit design generates nearly no force to the wire. For the tendon-mortise slits design, it generated force on bending, and the magnitude is also higher than the other type. This clearly demonstrates the high rigidity and stiffness of our design.

B. Algorithm Validation

Before putting the kinematics into practice, the optimization-based inverse kinematics should be first validated theoretically. We set 30 path points to follow, and system should find the optimal actuation inputs to match the tip point to the targets. The path points are radially distributed with a radius of $15mm$ and the value in z axis is $60mm$, so the rigid robot should translate adapt the z coordinate. First, the rotary DoF φ_d was set to zero. The shape and tip points are shown in Fig. 5 (a). Conversely, when it was activated, the shape could present more solution to reach the targets, as shown in Fig. 5 (b). Obviously, robot has multiple shapes with the tip at the given point if the two segments are allowed to be spatial arches. In terms of computation resource, the first set just takes $0.56s$ at most, and the second one takes $0.18s$ for each point search, which run on MATLAB 2021a Optimization Toolbox.

C. Path-Following Task

After evaluating the stiffness and the kinematics in simulation, the system was then tested to verify the performance. Six path points located within the task space were prepared to investigate the path-following accuracy. Two magnetic sensors were symmetrically configured at the tip of the distal segment, and another two magnetic sensors were placed symmetrically at the end of the proximal segment. There mean value was computed as the tip position and the initial base position, respectively, which were also deemed as actual position for comparison with the desired path points' position. For this task, experimental setup is shown in Fig. 6. The Electromagnetic tracking system (Aurora, NDI, Canada) monitored the position in real time. The six path points evenly distributed as a circle with the radius of $30mm$ and the value in z coordinate was $60mm$.

Initially, CAST was well calibrated and was vertically hang in the rigid robot arm. The relationship between actual pushing/pulling distance and bending angle was the key in calibration. After comparison with (3), the actual mapping

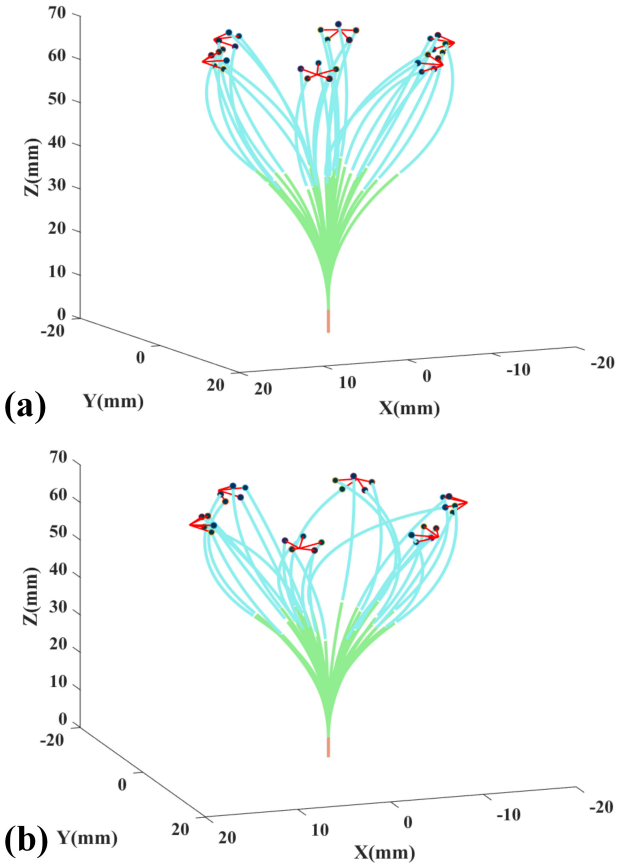

Fig. 5. Algorithm validation. (a)/(b) The rotary DoF of the distal segment was deactivated/activated.

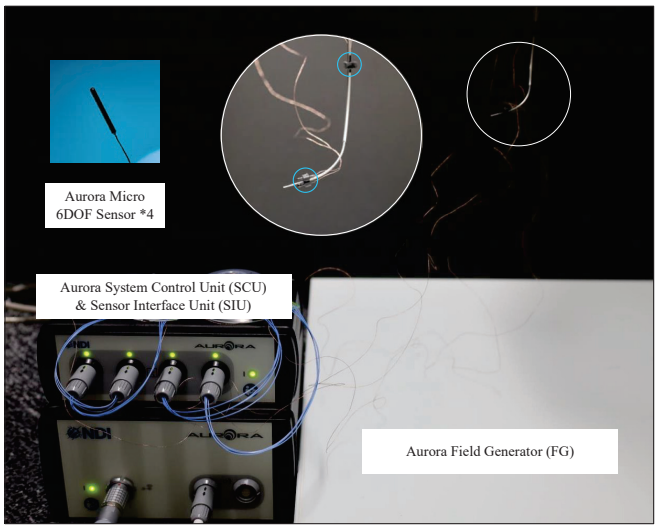

Fig. 6. Setup for path-following validation. Robot tip location from Electromagnetic tracking system (SCU, SIU, FG and Sensors).

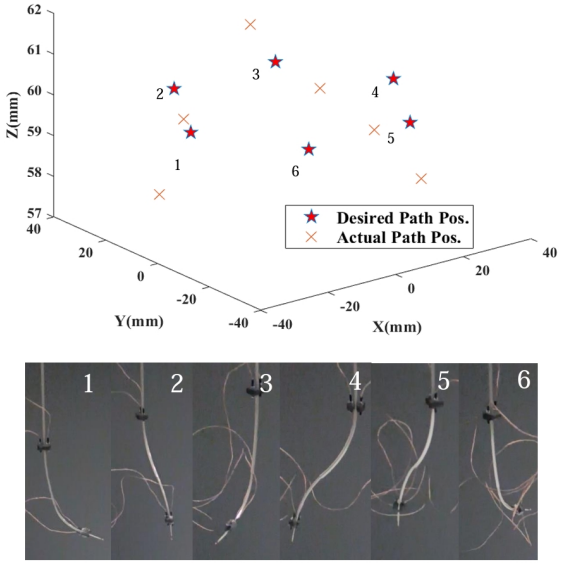

Fig. 7. Comparison with Designed Marker and Tip Position

was corrected by the collected data. During motion, the velocity of the rigid robot arm was very minimal, so the effect of inertial could be ignored.

Fig. 7 shows the given desired path points compared the actual ones and the posture of the robot at each waypoint, from which the position error was around $2mm$. In the third path point, the deviation between the actual and the desired reached to $3mm$, which was the maximum deviation in the test. This is the asymmetry of the flexible arm due to manufacturing discrepancy. The position error in other path points were all smaller than $2mm$, which could be used in surgery. With the length of entire flexible arm reaches $70mm$, the error is acceptable. The actual values were only used for evaluating the accuracy, and we believe the accuracy will be much higher if the actual values were to used as feedback for closed-loop control. In addition, the computation cost for each control instance was shorter than $0.4s$, which is applicable for MIS.

D. Application in TNS

Furthermore, the entire system was prepared to simulate one of the TNS procedures, electrocoauglation. A teaching-oriented skull model was fixed on a board, and a hole (diameter of $6mm$) was then drilled in the orbit for accessing the intracranial section. Inside the skull, a porcine tissue was adhered on the lateral surface. The experimental setup is shown in Fig. 8 (a).

The system was controlled in master-slave mechanism. A operator held a joystick to individually control the motion of each DoF, and the whole process was also recorded in the supplementary video. The rigid robot arm gradually brought CAST to approach the burr hole, and operator delicately tuned the orientation to be perpendicular with the hole.

Now, the orientation of the rigid robot arm keeps unchanged, and only translation along the CAST was activated.

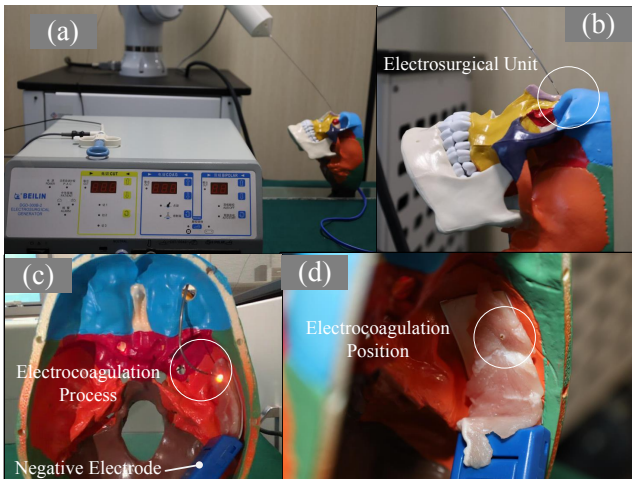

Fig. 8. Experimental setup for simulating the one of the actual TNS procedures. (b) CAST passes through a drilled hole in orbit. (c) Electrocoauglation process inside the skull.

Fig. 8 (b) shows the view when CAST approached the burr hole. Once the tip of CAST entered the hole, the distal segment started to bend to reach the simulated lesion area. Simultaneously, the proximal segment was also controlled to bypass the blocks. After arriving the area, the operator turned on the eletrosurgical generator (DGD-300B-2, Beilin, Beijing, China) and eletrocoagulation occurred, as shown in Fig. 8 (c).

Finally, the operator delicately controlled CAST to move out of the skull, avoiding touch with surroundings. It demonstrates the feasibility and practicability of the system, which achieved robotized operation of transorbital surgery.

V. CONCLUSION

This work proposed a robotic system, CAST, for TNS. One of the key novelties is co-axial tubular robot arm with tendon-mortise slits, which characterizes high stiffness as compared with conventional designs. The co-axial tube setting leaves much hollow space for instrument channel. Mounted it on a rigid robot arm that are for approaching the patient, the dexterity and automation degree are both improved significantly. In terms of control accuracy, we have proposed the kinematics and validated it to be $2mm$ in an open-loop controller. The modeling and control performance will be much better with feedback control schemes. Evaluation on a skull demonstrates the feasibility of the whole system. The success of electrocoauglation process inside the skull also shows the advantages: miniaturization, stiff, and dexterous.

In the future, both the theoretical model of this robot arm and hardware will be updated, and various tools like biopsy, endoscopic cameras and forceps will be mounted for more TNS surgery.

REFERENCES

[1] R. Ramakrishna, L. J. Kim, R. A. Bly, K. Moe, and M. Ferreira Jr, "Transorbital neuroendoscopic surgery for the treatment of skull base lesions," *Journal of Clinical Neuroscience*, vol. 24, pp. 99–104, 2016.

[2] K. S. Moe, C. M. Bergeron, and R. G. Ellenbogen, "Transorbital neuroendoscopic surgery," *Operative Neurosurgery*, vol. 67, no. 3, pp. ons16–ons28, 2010.

[3] L. M. Houlihan, A. J. S. Knoll, P. Kakodkar, X. Zhao, M. G. OâĂŹSullivan, M. T. Lawton, and M. C. Preul, "Transorbital neuroendoscopic surgery as a mainstream neurosurgical corridor: a systematic review," *World Neurosurgery*, vol. 152, pp. 167–179, 2021.

[4] D. Locatelli, F. Pozzi, M. Turri-Zanoni, P. Battaglia, L. Santi, I. Dallan, and P. Castelnuovo, "Transorbital endoscopic approaches to the skull base: current concepts and future perspectives," *Journal of neurosurgical sciences*, vol. 60, no. 4, p. 514âĂŤ525, December 2016. [Online]. Available: http://europepmc.org/abstract/MED/27280546

[5] V. G. HernÃąndez-Valderrama, R. M. Ordorica-Flores, S. Montoya-Alvarez, D. Haro-Mendoza, L. Ochoa-Toledo, D. Lorias-Espinoza, J. L. Ortiz-SimÃşn, and F. PÃľrez-Escamirosa, "Steerable surgical instrument for conventional and single-site minimally invasive surgery," *Surgical Innovation*, vol. 29, no. 3, pp. 449–458, 2022.

[6] T. da Veiga, J. H. Chandler, P. Lloyd, G. Pittiglio, N. J. Wilkinson, A. K. Hoshiar, R. A. Harris, and P. Valdastri, "Challenges of continuum robots in clinical context: a review," *Progress in Biomedical Engineering*, vol. 2, no. 3, p. 032003, 2020.

[7] D. A. Troncoso, J. A. Robles-Linares, M. Russo, M. A. Elbanna, S. Wild, X. Dong, A. Mohammad, J. Kell, A. D. Norton, and D. Axinte, "A continuum robot for remote applications: From industrial to medical surgery with slender continuum robots," *IEEE Robotics & Automation Magazine*, 2022.

[8] C. Shi, X. Luo, P. Qi, T. Li, S. Song, Z. Najdovski, T. Fukuda, and H. Ren, "Shape sensing techniques for continuum robots in minimally invasive surgery: A survey," *IEEE Transactions on Biomedical Engineering*, vol. 64, no. 8, pp. 1665–1678, 2016.

[9] X. Wei, F. Ju, H. Guo, B. Chen, and H. Wu, "Modeling and control of cable-driven continuum robot used for minimally invasive surgery," *Proceedings of the Institution of Mechanical Engineers, Part H: Journal of Engineering in Medicine*, vol. 237, no. 1, pp. 35–48, 2023.

[10] J. Zhang, Q. Fang, P. Xiang, D. Sun, Y. Xue, R. Jin, K. Qiu, R. Xiong, Y. Wang, and H. Lu, "A survey on design, actuation, modeling, and control of continuum robot," *Cyborg and Bionic Systems*, vol. 2022, 2022.

[11] M. Srivastava and I. D. Walker, "On tendon driven continuum robots with compressible backbones," in *2023 IEEE International Conference on Robotics and Automation (ICRA)*. IEEE, 2023, pp. 669–675.

[12] M. E. Smith, D. S. Esser, M. Rox, A. Kuntz, and R. J. Webster, "A radial folding mechanism to enable surgical continuum manipulators to fit through smaller ports," in *2023 International Symposium on Medical Robotics (ISMR)*. IEEE, 2023, pp. 1–6.

[13] D. Dragone, F. F. Donadio, C. Mirabelli, C. Cosentino, F. Amato, P. Zaffino, M. F. Spadea, D. La Torre, and A. Merola, "Design and experimental validation of a 3d-printed embedded-sensing continuum robot for neurosurgery," *Micromachines*, vol. 14, no. 9, p. 1743, 2023.

[14] K. Wen and J. Burgner-Kahrs, "Modeling and analysis of tendon-driven parallel continuum robots under constant curvature and pseudo-rigid-body assumptions," *Journal of Mechanisms and Robotics*, vol. 15, no. 4, p. 041003, 2023.

[15] T. Kato, I. Okumura, H. Kose, K. Takagi, and N. Hata, "Extended kinematic mapping of tendon-driven continuum robot for neuroendoscopy," in *2014 IEEE/RSJ International Conference on Intelligent Robots and Systems*. IEEE, 2014, pp. 1997–2002.

[16] Y. Li, T. Ren, Y. Chen, and M. Z. Chen, "A variable stiffness soft continuum robot based on pre-charged air, particle jamming, and origami," in *2020 IEEE International Conference on Robotics and Automation (ICRA)*. IEEE, 2020, pp. 5869–5875.

[17] Y. Roh, Y. Lee, D. Lim, D. Gong, S. Hwang, M. Kang, D. Kim, J. Cho, G. Kwon, D. Kang *et al.*, "Nature's blueprint in bioinspired materials for robotics," *Advanced Functional Materials*, p. 2306079, 2023.

[18] P. Wang, S. Guo, X. Wang, and Y. Wu, "Design and analysis of a novel variable stiffness continuum robot with built-in winding-styled ropes," *IEEE Robotics and Automation Letters*, vol. 7, no. 3, pp. 6375–6382, 2022.

[19] K. Oliver-Butler, J. A. Childs, A. Daniel, and D. C. Rucker, "Concentric push–pull robots: Planar modeling and design," *IEEE Transactions on Robotics*, vol. 38, no. 2, pp. 1186–1200, 2021.

[20] K. Oliver-Butler, Z. H. Epps, and D. C. Rucker, "Concentric agonist-antagonist robots for minimally invasive surgeries," in *Medical Imaging 2017: Image-Guided Procedures, Robotic Interventions, and Modeling*, vol. 10135. SPIE, 2017, pp. 270–278.

[21] F. Qi, F. Ju, D. Bai, Y. Wang, and B. Chen, "Kinematic analysis and navigation method of a cable-driven continuum robot used for minimally invasive surgery," *The International Journal of Medical Robotics and Computer Assisted Surgery*, vol. 15, no. 4, p. e2007, 2019.

[22] C.-H. Kuo, Y.-C. Chen, and T.-Y. Pan, "Continuum kinematics of a planar dual-backbone robot based on pseudo-rigid-body model: formulation, accuracy, and efficiency," in *International Design Engineering Technical Conferences and Computers and Information in Engineering Conference*, vol. 58172. American Society of Mechanical Engineers, 2017, p. V05AT08A015.

[23] J. Till, V. Aloi, and C. Rucker, "Real-time dynamics of soft and continuum robots based on cosserat rod models," *The International Journal of Robotics Research*, vol. 38, no. 6, pp. 723–746, 2019.

[24] D. Alatorre, D. Axinte, and A. Rabani, "Continuum robot proprioception: the ionic liquid approach," *IEEE Transactions on Robotics*, vol. 38, no. 1, pp. 526–535, 2021.